Title

Non-contrast-enhanced peripheral angiography using a sliding interleaved cylinder acquisition

Permalink

https://escholarship.org/uc/item/8kn3z7j9

Journal

Magnetic Resonance in Medicine, 74(3)

ISSN

0740-3194

Authors

Kwon, Kie Tae
Kerr, Adam B
Wu, Holden H
et al.

Publication Date

2015-09-01

DOI

10.1002/mrm.25452

Published in final edited form as:
Magn Reson Med. 2015 September ; 74(3): 727–738. doi:10.1002/mrm.25452.

Non-contrast-enhanced Peripheral Angiography Using a Sliding Interleaved Cylinder Acquisition

Kie Tae Kwon[1], **Adam B. Kerr**[1], **Holden H. Wu**[2], **Bob S. Hu**[3], **Jean H. Brittain**[4], and **Dwight G. Nishimura**[1]

[1]Magnetic Resonance Systems Research Laboratory, Department of Electrical Engineering, Stanford University, Stanford, California, USA

[2]Department of Radiological Sciences, University of California at Los Angeles, Los Angeles, California, USA

[3]Cardiovascular Medicine, Palo Alto Medical Foundation, Palo Alto, California, USA

[4]Department of Radiology, University of Wisconsin-Madison, Wisconsin, USA

Abstract

Purpose—To develop a new sequence for non-contrast-enhanced peripheral angiography using a sliding interleaved cylinder (SLINCYL) acquisition.

Methods—A venous saturation pulse was incorporated into a 3D magnetization-prepared balanced steady-state free precession sequence for non-contrast-enhanced peripheral angiography to improve artery-vein contrast. The SLINCYL acquisition, which consists of a series of overlapped thin slabs for volumetric coverage similar to the original sliding interleaved k_y (SLINKY) acquisition, was employed to evenly distribute the venous-suppression effects over the FOV. In addition, the thin-slab-scan nature of SLINCYL and the centric-ordered sampling geometry of its readout trajectory were exploited to implement efficient fluid-suppression and parallel imaging approaches. The sequence was tested in healthy subjects and a patient.

Results—Compared to a multiple overlapped thin slab acquisition, both SLINKY and SLINCYL suppressed the venetian blind artifacts and provided similar artery-vein contrast. However, SLINCYL achieved this with shorter scan times and less noticeable artifacts from k-space amplitude modulation than SLINKY. The fluid-suppression and parallel imaging schemes were also validated. A patient study using the SLINCYL-based sequence well identified stenoses at the superficial femoral arteries, which were also confirmed with digital subtraction angiography.

Conclusion—Non-contrast-enhanced angiography using SLINCYL can provide angiograms with improved artery-vein contrast in the lower extremities.

Keywords

Non-contrast-enhanced; peripheral angiography; SLINKY; SLINCYL; 3D concentric cylinders; bSSFP

Address correspondence to: Kie Tae Kwon M.S. Packard Electrical Engineering, Room 208 350 Serra Mall Stanford, CA 94305-9510 TEL: (650) 725-5638 ktkwon07@stanford.edu.

Introduction

Magnetic resonance angiography (MRA) is an important clinical tool for the diagnosis and management of arterial diseases. Contrast-enhanced (CE) MRA uses gadolinium-based contrast agents to reduce the T_1 of blood, and has been widely accepted for many applications due to its rapid acquisition of high contrast angiograms (1–4). New types of agents such as blood-pool agents (5) have been also developed to prolong the effect of the agents to achieve higher spatial resolution and/or signal-to-noise ratio (SNR) than conventional first-pass agents.

However, intravenous administration of contrast agents increases exam costs, which can become significant, especially in areas of the world with low reimbursement rates. In addition, the potential risk of nephrogenic systemic fibrosis (NSF) linked with gadolinium-based contrast agents makes it desirable to have non-contrast alternatives for imaging of patients with renal impairment (6–8).

Non-contrast-enhanced (NCE) MRA has regained interest recently due to the aforementioned issues with CE MRA (8). Most NCE MRA methods take advantage of relatively fast flowing arterial blood to achieve sufficient contrast. These flow-dependent methods include phase-contrast (PC) (9), time-of-flight (TOF) (10, 11), velocity-selective imaging (12, 13), fresh blood imaging (FBI) (14), and other subtractive imagings based on flow-induced intravoxel dephasing effects (15,16).

However, concerns with NCE flow-dependent MRA methods include the sensitivity to trigger delay timing and the possibility of reduced arterial flow rates and pulsatility, which are typically the case in the lower extremities. A recently proposed flow-dependent method, called quiescent-interval single-shot (QISS) imaging, is robust to these issues and achieves comparable image quality to CE MRA in the lower extremities with relatively short scan time (17). However, because the robustness of this 2D multi-slice approach is based on the time-of-flight effect during a relatively short quiescent interval, its application to 3D volumetric imaging for higher resolution in the slice direction and/or higher SNR would be limited.

On the other hand, NCE flow-independent MRA methods exploit intrinsic tissue parameters such as T_1, T_2 and chemical shift to suppress background signals and generate vessel contrast (18–21). Unlike most flow-dependent methods, flow-independent methods can generate stable vessel contrast even with slow flow in the lower extremities. Magnetization-prepared 3D balanced steady-state free precession (bSSFP) sequences have been of interest for flow-independent methods (22,23) due to bSSFP's high SNR efficiency and bright blood signal (24). However, it can be difficult to generate sufficient artery-vein contrast in the lower extremities using these sequences, considering that the T_2 of deep venous blood is found to be closer to that of deep arterial blood in some patients with peripheral vascular diseases (22,25).

In this work, we developed an NCE peripheral MRA sequence using a sliding interleaved cylinder (SLINCYL) acquisition (26). The SLINCYL acquisition is a variation of a sliding interleaved k_y (SLINKY) (27) acquisition in which a 3D concentric cylinders trajectory (28–

31) is used as the readout instead of a 3D Cartesian (3DFT) sequence. Compared to SLINKY, SLINCYL offers faster scan times and more distributed artifacts from k-space amplitude modulation.

In the new sequence, a venous saturation pulse is incorporated into a 3D magnetization-prepared bSSFP sequence to improve artery-vein contrast in the lower extremities. The SLINCYL acquisition is employed to evenly distribute the venous-suppression effects over the FOV. In addition, the thin-slab-scan nature of SLINCYL and the centric-ordered sampling geometry of its readout trajectory are exploited to implement efficient fluid-suppression and parallel imaging approaches (32, 33). In vivo experiments in healthy subjects and a patient with arterial stenosis demonstrate that the SLINCYL-based sequence can provide improved artery-vein contrast.

Theory

3D Concentric Cylinders Trajectory

A 3D concentric cylinders trajectory (28–31) is a hybrid that offers a favorable balance between Cartesian and non-Cartesian sampling properties. It consists of a set of N_{cy} uniformly spaced cylinders (index of cylinders starts from 1, indicating the innermost cylinder), with each cylinder uniformly covered by a set of N_{intlv} helical interleaves with N_{rev} revolutions (Fig. 1a). Each helical interleaf is generated by a constant G_z gradient and oscillating G_x and G_y gradients during the readout. The G_x and G_y gradients are designed for the outermost cylinder and then scaled down for the inner cylinders to achieve robustness to off-resonance effects and timing delays, which manifest as a benign geometric shift in the z direction and a bulk in-plane rotation, respectively (30,31).

The matrix size of the reconstructed image after gridding is $2N_{cy} \times 2N_{cy} \times N_{slice}$, where $N_{slice} = N_{intlv} \times N_{rev}$. In this sense, concentric cylinders require a factor of $2N_{rev}$ fewer excitations and shorter scan times than a comparable 3DFT sequence. The reduction factor of scan time is typically not as high as $2N_{rev}$ due to the longer readout duration ($\propto N_{rev}$) and pulse repetition time (TR) compared to 3DFT.

Sliding Interleaved Cylinder (SLINCYL) Acquisition

A SLINCYL acquisition is a variation of a SLINKY (27) acquisition in which the 3D concentric cylinders trajectory is used as the readout instead of a 3DFT sequence. Similar to SLINKY, SLINCYL consists of a series of overlapped thin slabs for volumetric coverage, where the slab location is incremented by a distance equal to the resolution in the slab direction (d in Fig. 1b). Each thin slab consisting of N_{slice} slices (thus $N_{slice} \times d$ thick) has a different 3D k-space from which one of N_s interleaved subsets of concentric cylinders (instead of k_y lines for SLINKY) is collected. More specifically, slab j (j starts from 1, indexed sequentially in the slab direction from superior to inferior) collects a partial set of cylinders with indices: $1 + ((j - 1) \bmod N_s) + k \times N_s$, where integer $k = 0, 1, ..., N_{cy}/N_s - 1$ (N_s chosen as a divisor of N_{cy}). With this assignment, each interleaved subset of cylinders repeats every N_s slabs. Figure 1b illustrates the case with $N_{cy} = 12$ and $N_s = 4$.

Although each slab is undersampled in cylinders (in k_x and k_y), its collected cylinders are still fully sampled in k_z. With N_{samp} (# of sampling points per interleaf) chosen as an integer multiple of N_{slice}, each sampling point of a collected cylinder is aligned in the k_z direction with other $N_{slice} - 1$ points (Fig. 1c). By directly applying a 1D inverse Fourier transform in k_z to each group of aligned sampling points and correcting the linear phase induced by the shift in k_z (w in Fig. 1c), N_{slice} undersampled hybrid slices (k_x k_y z) are generated from each slab without aliasing in z.

To reconstruct a slice, its relevant hybrid slices are first selected out of N_s consecutive slabs. Figure 2a illustrates the case with $N_{cy} = 72$ and $N_s = 24$. After combining those N_s hybrid slices to form a fully sampled slice, 2D gridding is performed, which is followed by a 2D inverse Fourier transform in k_x and k_y to finally reconstruct the slice in the image domain ($x - y - z$). In this sense, the final number of slices reconstructed from N_{slab} ($\geq N_s$) slabs is $N_{slab} - (N_s - 1)$ (27). With the use of a linear-phase radiofrequency (RF) pulse, k-space phase modulation is negligible across the N_s consecutive slabs from which a slice is reconstructed, and the artifacts due to the data inconsistency can be minimized (34).

Parallel Imaging With SLINCYL

During the reconstruction steps described in the previous section, the k-space data of each slice remain on the original non-Cartesian sampling points in the k_x-k_y plane before 2D gridding is performed. Therefore, a 2D non-Cartesian parallel imaging method can be applied to each slice individually, with data consistency enforced to or evaluated with the k-space data using 2D gridding/inverse gridding pairs.

Undersampling is achieved by collecting cylinders fewer than necessary for full FOV in the x-y plane from each N_s consecutive slab. For the collected cylinders, all helical interleaves need to be acquired to maintain full sampling in k_z. Figure 1d illustrates one way of undersampling for the case in Fig. 1b. While the fully sampled acquisition map (top) collects a full set of $N_{cy} = 12$ cylinders from $N_s = 4$ consecutive slabs, the undersampled map (bottom) aimed for a reduction factor $R = 2$ does not collect cylinders with indices 6, 8, 10, and 12 by skipping every other slab. As the autocalibration signal (ACS) region, the four innermost cylinders are fully sampled, which decreases the effective R. The corresponding undersampling pattern of the k-space data in each slice is shown in Fig. 1e.

SLINKY vs. SLINCYL

Compared to SLINKY, SLINCYL offers faster scan times (3DFT vs. cylinders). In addition, SLINCYL provides more distributed artifacts from k-space amplitude modulation while similarly suppressing venetian blind artifacts, which is demonstrated in this section.

The main purpose of the sliding acquisitions of SLINKY and SLINCYL is to suppress venetian blind artifacts by transforming in flow enhancement into k-space amplitude modulation (27). With sliding acquisitions, each of N_s hybrid slices that are combined to form a fully sampled slice has a different distance to the flow-entering boundary of its corresponding slab (Fig. 2a). Therefore, each hybrid slice experiences a different degree of in flow enhancement, which typically decreases with distance into the slab (Fig. 2b, left).

When combined to form a fully sampled slice, the variable enhancement manifests as a periodic k-space amplitude modulation with the period equal to N_s, which is along k_y for SLINKY and along k_r (radial direction) for SLINCYL (Fig. 2b, right).

The point spread functions (PSFs) due to the k-space amplitude modulation patterns in Fig. 2b were calculated with the imaging parameters for thighs listed in Table 1 to compare SLINKY and SLINCYL. Because the modulation pattern is circularly shifted for adjacent slices and repeats every N_s slices, it is sufficient to consider only a set of N_s consecutive slices for the comparison.

The ratio of the maximum amplitude uctuation to the maximum amplitude of the modulation patterns used for the calculation was set to 0.5. As noted in Liu et al. (27), the ratio almost never exceeds 0.5 in practice, and hence the comparison would show how well SLINKY and SLINCYL perform even for the most extreme case.

Compared to SLINKY (Fig. 2c), the PSFs of SLINCYL (Fig. 2d) show more distributed artifacts over the *x*-*y* plane. In the first slice (left/middle columns), the highest ghost amplitude is 10.5% of the main lobe with SLINKY, whereas it is reduced to 2.4% with SLINCYL. This reduction is consistently observed across the PSFs of $N_s = 24$ slices (right columns).

The full-width at half-maximum of the main lobe of SLINCYL is 15% broader than SLINKY due to its circular (instead of square for SLINKY) coverage of k-space in the k_x-k_y plane (35), and this results in a reduction in resolution. Depending on other reconstruction processes such as windowing or zero-filling (36), up to 15% more cylinders may need to be collected to match the resolution with SLINKY. Even with the broadening, the peak amplitude of the main lobe is still quite uniform across $N_s = 24$ slices (right in Fig. 2d), where the coefficient of variation (CV) is 0.9%.

In addition, the signal levels across $N_s = 24$ slices simulated with different vessel radii (Fig. 2e) show that SLINCYL also provides relatively uniform signal levels for vessels with radius up to 7 mm, which is the range of radius typically observed in the lower extremities (37). The maximum CV is 2.1%, which is still a factor of 10 less than that of the in flow-enhancement profile used in the simulation (Fig. 2b). Although not as constant as SLINKY, the much improved uniformity demonstrates that SLINCYL also effectively suppresses the venetian blind artifacts by equalizing the inflow-enhancement effects across the slab direction.

NCE Magnetization-Prepared 3D bSSFP Peripheral Angiography With SLINCYL

The SLINCYL acquisition is used for an NCE magnetization-prepared 3D bSSFP peripheral angiography (abbreviated to SLINCYL MRA). Figure 3a shows the basic pulse sequence block (block P) (31) for each slab of SLINCYL MRA. It starts with a venous saturation pulse that saturates a region inferior to the FOV to help suppress venous blood flowing into the FOV. Because of slow venous flow, this venous-suppression scheme dictates the thickness of each slab. Next, a spectral fat saturation pulse is applied, which is followed by a segment of bSSFP SLINCYL readouts surrounded with ramp-in/out catalyzations. Finally, a recovery time $T_{recovery}$ is given in the end. The SLINCYL readouts are employed to evenly distribute the venous-suppression as well as arterial-inflow-enhancement effects across the S/I direction. The readouts of each slab are divided into N_{seg} centric-ordered segments (i.e., the innermost cylinder is acquired first), where N_{seg} is chosen to provide an acquisition window (T_{acqwnd}) sufficiently short to capture the transient contrast generated from venous/fat saturation pulses. In this manner, block P repeats N_{seg} times for each slab before moving to the next slab in the S/I direction.

Fluid Suppression For SLINCYL MRA

SLINCYL MRA with the basic pulse sequence block (block P) in the previous section does not take into account long-T_1 fluids such as synovial fluid or edema in the lower extremities, which can hamper the depiction of blood vessels in the bSSFP images due to their higher T_2/T_1 ratios (e.g., 1210/2850 ms for synovial fluid, 254/1273 ms for arterial blood, and 50/870 ms for muscle at 1.5 T (18, 38, 39)). An additional pulse sequence block (block Q) shown in Fig. 3b is employed to address this issue (23,40). It consists of two components: i) a selective inversion pulse (41) with a subsequent inversion delay of TI to suppress long-T_1 fluids, and ii) an adiabatic B_1-insensitive rotation (BIR-4) pulse (42) for T_2-preparation to suppress muscle that is almost fully recovered after the inversion delay.

Considering the long T_1 of targeted fluids and the typical span of acquisition windows during N_{seg} repetitions of block P (< 3 s), it is sufficient to apply block Q only once per each slab as shown in Fig. 3c (31). However, it still requires relatively long TI (~ 2 s) and recovery time $T_{recovery,Q}$ (> 3 s, Fig. 3c), which together at least double the scan time. To maintain a reasonable scan time, two modifications are made to the SLINCYL MRA scheme.

First, the assignment of an interleaved subset of cylinders to each slab is modified such that block Q can be applied less frequently (once per every N_g slabs) while the signal level of suppressed fluids is still lower than that of arterial blood. With N_g chosen as a divisor of N_s, slab j now collects cylinders with modified indices: $1 + \lfloor ((j-1) \bmod N_s)/N_g \rfloor + ((j-1) \bmod N_g) \times N_s/N_g + k \times N_s$, where integer $k = 0, 1, \ldots, N_{cy}/N_s - 1$. An example is illustrated in Fig. 3d with $N_s = 6$, $N_g = 3$, and $N_{cy} = 18$. With this new assignment, block Q is selectively applied ahead of the slabs that collect the N_s/N_g innermost cylinders (closest to the center of the k-space), which reduces the number of block Q by a factor N_g while capturing the contrast more effectively than the original sequential assignment.

Second, the order of the acquisition of slabs are modified such that the explicit recovery time $T_{recovery,Q}$ for block Q is no longer necessary. After a set of N_g slabs is acquired as described in the previous paragraph, the next set of N_g slabs is chosen such that there is no overlap between those two sets of slabs, including their saturated regions for venous suppression. An example is illustrated in Fig. 3e, where N_{slab} = 180 slabs are acquired by interleaving the lower/upper half of the slabs. With this modification, the time for acquiring each set of N_g slabs can replace $T_{recovery,Q}$ of the previous set, which was originally required for sufficient recovery of long-T_1 fluids inverted by the selective inversion pulse in block Q.

With these modifications, the additional time for fluid suppression is N_{slab}/N_g × (TI +TE_{prep}), which is much shorter than the additional time N_{slab} × (TI+TE_{prep}+$T_{recovery,Q}$) associated with the original fluid-suppression scheme (Fig. 3c).

Methods

In Vivo Experiments

In vivo experiments of SLINCYL MRA were performed on four healthy subjects and a patient with arterial stenosis. Informed written consent approved by our institutional review board was obtained from all subjects prior to scanning. All experiments were conducted on 1.5 T scanners (Signa Excite; GE Healthcare, Waukesha, WI, USA) with maximum gradient amplitude of 40 mT/m and maximum slew rate of 150 mT/m/ms. No cardiac triggering was used. Unless otherwise noted, an eight-channel receiver-coil array was used and the following sequence parameters were common to all experiments described in this section: slab-acquisition direction = superior to inferior, venous saturation pulse applied to a 6.4 cm-thick slab whose superior boundary is 4 mm inferior to the inferior boundary of the imaging FOV (for the transition band of the saturation pulse with time-bandwidth product 24), 1.6 ms sinc pulse for excitations, T_{prep} = 50 ms, T_{cat} = 10 TRs, and $T_{recovery}$ = 100 ms (Fig. 3a). The thickness of the venous saturation band was based on the venous velocity in the lower extremities (< 10 cm/s) (43) and the maximum time gap between the saturation pulse and the following readout segment (< 0.6 s). SLINCYL sequence parameters that were chosen differently for thighs and calves are summarized in Table 1. The parallel imaging and/or fluid-suppression schemes were used only when explicitly mentioned.

First, two sets of experiments imaging the thighs and calves of healthy subjects were performed to compare SLINCYL with previously proposed methods, i.e., SLINKY and a multiple overlapped thin slab acquisition (MOTSA) (44). A quadrature birdcage coil was used for calves. For SLINCYL, 168 slabs were acquired to cover 20(thighs)/17(calves) cm in the S/I direction. Additional datasets without venous saturation pulse were also acquired. For SLINKY, 168 slabs were acquired with the same sequence parameters as SLINCYL except for the parameters within brackets in Table 1. Among them, N_{seg} (= 3) was increased to provide a similar T_{acqwnd} as SLINCYL. Because the readout was in the R/L direction to minimize the number of phase encodings, it was not available to use a hard pulse that could otherwise shorten the TR of SLINKY with an aid of anti-aliasing filter in the S/I direction. The phase encodings were 1D centric-ordered in the A/P direction while $\mathrm{FOV}_{A/P}$ was halved. For MOTSA, seven slabs with 12 slices overlapped between adjacent slabs were acquired to provide the same coverage and scan time as SLINKY. Except for the increased N_{seg} (= 72) to provide the same T_{acqwnd} as SLINKY, other parameters were equal to SLINKY.

Second, a set of experiments imaging the calves of a healthy subject was performed using a quadrature birdcage coil to demonstrate the feasibility of the proposed fluid-suppression scheme using block Q. The degree of fluid suppression was compared among acquisitions with different N_g (3/4/6/12) and an acquisition without fluid suppression. 168 slabs were acquired for each scan. For the acquisitions with fluid suppression, additional sequence parameters (Fig. 3b) were: TI = 1.9 s and TE_{prep} = 40 ms.

Third, a set of experiments imaging the calves of a healthy subject was performed to demonstrate the feasibility of the proposed parallel imaging scheme. The image quality was compared between a fully sampled and a prospectively undersampled ($R = 2$) SLINCYL acquisition. For the fully sampled case, 168 slabs were acquired. For the undersampled case, only 84 slabs with a doubled increment between slabs ($d = 2.4$ mm instead of 1.2 mm in Fig. 1b) were acquired to achieve the same coverage. The 24 innermost cylinders were fully sampled as the ACS region for calibrating a 9 × 9 kernel for iterative self-consistent parallel imaging reconstruction (SPIRiT) (45).

Fourth, sets of experiments imaging both the thighs and calves of healthy subjects were performed to demonstrate the feasibility of SLINCYL MRA that integrates the aforementioned techniques (fluid suppression/parallel imaging with $R = 2$). 120(thighs)/136(calves) slabs with a doubled increment between slabs were acquired to cover 30 cm in the S/I direction for each station. $N_g = 4$ was chosen based on the fluid-suppression experiment. For the calf station, a shorter TR (5.8 ms) compared to Table 1 was used to avoid banding artifacts.

Finally, an experiment imaging the thighs of a patient was performed to demonstrate the capability of SLINCYL MRA to deal with slow blood flow. The subject was referred for a digital subtraction angiography (DSA) examination with which SLINCYL MRA was compared. This dataset had been acquired before the parameters for thighs were established, and the following parameters were different from Table 1: $N_{slice} = 30$ ($FOV_{S/I} = 4.2$ cm), $N_{intlv} = 30$, $N_{rev} = 1$, $N_{seg} = 3$, and TR = 5.4 ms. 240 slabs were acquired to cover 30 cm in the S/I direction.

Image Analysis

For the first and second in vivo experiments, SNR measurements were performed on the manually selected regions of the source images. Arterial signal was measured around the femoral arteries for thighs and the popliteal/tibial arteries for calves. Also, venous signal from the deep vein and muscle signal near the arterial regions were measured. Fluid signal was measured around the knee joint. The noise standard deviation was estimated from the image background. The same regions were measured for different acquisitions. Paired, two-tailed Student's t-tests were performed with 0.005 chosen as the significance level.

Results

Unless otherwise noted, all the in vivo results are shown as targeted coronal maximum-intensity-projection (MIP) images with a factor of two zero-padding in all dimensions (46).

SLINCYL vs. SLINKY vs. MOTSA

Figure 4 shows the results of comparing SLINCYL with SLINKY and MOTSA. Compared to SLINCYL without venous saturation pulse (Fig. 4a and e), SLINCYL with venous saturation pulse (Fig. 4b and f) significantly improves contrast between arteries and veins (mean CNR from 6.15/2.06 to 29.09/14.41 for thigh/calf, $P < 0.005$) without loss of arterial signal ($P > 0.005$). Compared to MOTSA (Fig. 4d and h) processed with the maximum overlapping pixel algorithm (47), both SLINKY (Fig. 4c and g) and SLINCYL successfully suppress the venetian blind artifacts and provide similar artery-vein contrast (mean CNR 33.72/14.23 for SLINKY vs. 29.09/14.41 for SLINCYL). However, SLINCYL achieves this with shorter scan times than SLINKY, as summarized in Table 2 (on average 67% of SLINKY). In addition, the artifacts of SLINCYL (Fig. 4i) are less noticeable than those of SLINKY (Fig. 4j), which is consistent with the simulation results in Fig. 2.

Fluid Suppression

Figure 5 shows the results of comparing the degree of fluid suppression among different SLINCYL acquisitions. Compared to the acquisition without block Q (Fig. 5a), the acquisitions with block Q (Fig. 5b-e) provide better depiction of arterial signals due to the suppression of fluid signals around the knee joint. The degree of fluid suppression becomes better as block Q (Fig. 3b) is applied more frequently ($P < 0.005$). Arterial signal is also slightly decreased due to the T_2-preparation module ($P < 0.005$).

The SNR of fluid and arterial signals for different cases are summarized in Fig. 5f. Among them, $N_g = 4$ (Fig. 5d) provides an acceptable level of fluid suppression (i.e., no overlap of 95% confidence intervals between the arterial and fluid signals: [17.40, 24.42] vs. [7.05, 15.25]) with the additional scan time only 38% of the case without block Q. Figure 5g shows the Bloch simulations corresponding to this case and the case without block Q, which were simulated for eight SLINCYL readout segments. Proton densities were assumed to be the same for all the tissues. Without block Q (top), the signal level of joint fluid is higher than arterial blood (0.39 vs. 0.29). With block Q and $N_g = 4$ (bottom), joint fluid is suppressed and particularly becomes much lower than arterial blood for the readout segments corresponding to the first slab (0.07 vs. 0.25), which collects the six ($=N_s/N_g$) innermost cylinders.

Parallel Imaging

Figure 6 shows the results of comparing a fully sampled and a prospectively undersampled ($R = 2$) acquisition for parallel imaging. In addition to coronal MIP images (Fig. 6a and b), a representative axial slice (Fig. 6c and d) from each acquisition is shown. The prospectively undersampled acquisition reconstructed with the proposed parallel imaging scheme (Fig. 6b and d) shows comparable image quality to the fully sampled acquisition (Fig. 6a and c) other than the decrease in SNR. Total scan times were 3 min 35 s and 1 min 57 s for the fully sampled and undersampled cases, respectively.

Two-station SLINCYL MRA

Figure 7 shows the results of two-station SLINCYL MRA of a healthy subject in the lower extremities. The main arteries (femoral, popliteal, tibial, and peroneal) are well depicted across the FOV. The angiograms also show good overall background suppression of venous, muscle, and synovial fluid signals. Some fluid signal around the knee joint (Fig. 7b) was not sufficiently suppressed due to the increased (doubled) number of readouts per slab accompanied with a shorter TR. Total scan times were 3 min 25 s and 6 min 28 s for the thigh/calve stations, respectively.

Initial Patient Study

Figure 8 shows the result of the initial patient study (Fig. 8a) with a comparison to DSA (Fig. 8b). Although the spatial resolution (1.4 mm isotropic) was lower than that of DSA, SLINCYL MRA still identifies stenoses at the superficial femoral arteries and is also able to depict smaller vessels. Total scan time of SLINCYL MRA was 6 min.

Discussion

The structure of the proposed SLINCYL MRA is based on that of NCE flow-independent MRA with magnetization-prepared bSSFP (23). However, SLINCYL MRA also has its flown features that are different from the original flow-independent sequences. One of the most distinctive differences is that it employs a venous saturation pulse to improve artery-vein contrast. Although relying on the venous in flow, the sequence is tolerant of slow venous flow due to the SLINCYL readout which distributes the venous-suppression effects evenly across the slab direction. With its thin slabs, SLINCYL MRA takes advantage of increased arterial in flow enhancement, which is also equalized across the slab direction. However, it is still arterial flow independent considering that the arterial signal is not spatially saturated before the bSSFP readouts in the imaging FOV and bright blood signal can be achieved by the steady-state bSSFP contrast even with slow arterial flow.

The comparison study in Fig. 4 shows that SLINCYL can provide shorter scan times and suppressed venetian blind artifacts compared to MOTSA. The latter improvement was noticeable with arterial flow, but was almost unnoticeable with venous flow. This is probably due to the excitation pulses with a high flip angle (≥60°), which saturates the venous signals around the superior side of each thin slab. Still, MOTSA processed with the maximum overlapping pixel algorithm (47) may pick higher venous signals from the overlapped regions, which would undesirably decrease artery-vein contrast.

The fluid-suppression scheme of SLINCYL MRA was able to suppress synovial fluids around the knee joints effectively, but those fluids can be also removed by targeted coronal MIP (20). The fluid-suppression scheme might be more useful for the case when fluids such as edema have a diffuse distribution over the FOV. TI, which was set to 1.9 s based on the T_1 of synovial fluid, also needs to be changed accordingly. However, TI should not be made too short compared to the T_1 of arterial blood, because TI is also the time for the suppressed arterial blood (due to the venous saturation and excitation pulses applied to the superior side of the imaging FOV) to recover and/or pass the imaging FOV before the next readouts.

The parallel imaging scheme for SLINCYL reconstructs each slice individually, which is enabled by the tailored sampling geometry of the concentric cylinders that aligns the sampling points in the k_z direction. Otherwise, due to the lack of an ACS region for each slab, the entire 3D non-Cartesian dataset needs to be considered together, which would require extensive use of 3D gridding/inverse gridding pairs and may not be as efficient as the proposed scheme.

The initial patient study in Fig. 8 shows that SLINCYL MRA can generate stable vessel contrast even in a patient with arterial stenosis that could potentially reduce arterial and/or venous flow. The level of venous suppression was relatively uniform across the FOV, but may need to be improved for better diagnosis. Considering potentially lower venous in flow for a patient, this may necessitate i) a thinner slab and/or ii) a longer time gap between the venous saturation pulse and the readout. The degree of stenosis indicated by dashed arrows in Fig. 8 was overestimated with SLINCYL MRA compared to DSA. More systematic analysis on a cohort of patients with peripheral artery disease would be helpful to optimize sequence parameters and evaluate the sensitivity and specificity of SLINC MRA on identifying stenoses.

There are several potential limitations to SLINCYL MRA. First, although it is tolerant of slow venous flow, the venous-suppression scheme works only with the presence of flow in the slab (S/I) direction. Otherwise, the artery-vein contrast is dominantly from the steady-state bSSFP contrast. Second, it is vulnerable to bSSFP banding artifacts due to its relatively long TR. A shorter TR can help (Fig. 7b), but it reduces the scan time efficiency. One potential way to overcome this issue is to exploit the thin-slab-scan nature of the SLINCYL acquisition. The center frequency of each thin slab can be adjusted to reflect the average off-resonance frequency within the slab to reduce banding artifacts (48–50). A 2D coronal field map would need to be acquired to facilitate this enhancement. Third, only 24 of 32 slices of each slab are used in the reconstruction due to the limited time-bandwidth product (= 6) of the excitation pulse. The pulse can be designed to have a nonlinear phase distribution across the excitation slab while the phase dispersion within each slice is minimized (34). This may reduce the peak power of a sharper RF profile, which would increase the usage of each slab and scan time efficiency. Finally, an anisotropic in-plane FOV (51) may need to be considered for SLINCYL MRA to efficiently prescribe the FOV in the lower extremities as the rectangular FOV of a 3DFT sequence.

Conclusions

We have demonstrated the feasibility of SLINCYL MRA with a magnetization-prepared 3D bSSFP sequence for achieving improved artery-vein contrast in the lower extremities. Initial results show robust arterial contrast in healthy subjects and in a patient with arterial stenosis. The thin-slab-scan nature of the SLINCYL acquisition and the centric-ordered sampling geometry of its readout trajectory also facilitate novel fluid-suppression and parallel imaging approaches that improve the method's robustness and speed.

Acknowledgments

The authors thank Taehoon Shin and Pauline W. Worters for helpful discussions, and Joseph Y. Cheng for providing a gradient unwarping tool.

This work was supported by NIH (R01 HL075803, R01 HL039297) and GE Healthcare.

References

1. Prince M. Gadolinium-enhanced MR aortography. Radiology. 1994; 191:155–164. [PubMed: 8134563]
2. Korosec FR, Frayne R, Grist TM, Mistretta CA. Time-resolved contrast-enhanced 3D MR angiography. Magn Reson Med. 1996; 36:345–351. [PubMed: 8875403]

3. Wilman AH, Rossman J, King F, Debbins J, Rossman P, Ehman R. Fluoroscopically triggered contrast-enhanced three-dimensional MR angiography with elliptical centric view order: application to the renal arteries. Radiology. 1997; 205:137–146. [PubMed: 9314975]
4. Ruehm SG, Hany TF, Pfammatter T, Schneider E, Ladd M, Debatin JF. Pelvic and lower extremity arterial imaging: Diagnostic performance of three-dimensional contrast-enhanced MR angiography. AJR Am J Roentgenol. 2000; 174:1127–1136. [PubMed: 10749264]
5. Wolf F, Plank C, Beitzke D, Popovic M, Domenig CM, Weber M, Loewe C. Prospective evaluation of high-resolution MRI using gadofosveset for stent-graft planning: Comparison with CT angiography in 30 patients. AJR Am J Roentgenol. 2011; 197:1251–1257. [PubMed: 22021522]
6. Thomsen HS. Nephrogenic systemic brosis: A serious late adverse reaction to gadodiamide. Eur Radiol. 2006; 16:2619–2621. [PubMed: 17061066]
7. Kanal E, Barkovich AJ, Bell C, Borgstede JP, Bradley WG, Froelich JW, Gilk T, Gimbel JR, Gosbee J, KuhniKaminski E, Lester JW, Nyenhuis J, Parag Y, Schaefer DJ, SebekScoumis EA, Weinreb J, Zaremba LA, Wilcox P, Lucey L, Sass N. ACR guidance document for safe MR practices: 2007. AJR Am J Roentgenol. 2007; 188:1447–1474. [PubMed: 17515363]
8. Miyazaki M, Akahane M. Non-contrast enhanced MR angiography: Established techniques. J Magn Reson Imaging. 2012; 35:1–19. [PubMed: 22173999]
9. Dumoulin CL, Souza SP, Walker MF, Wagle W. Three-dimensional phase contrast angiography. Magn Reson Med. 1989; 9:139–149. [PubMed: 2709992]
10. Marchal G, Bosmans H, Fraeyehoven L, Wilms G, Hecke P, Plets C, Baert A. Intracranial and clinical lesions: Optimization and clinical evaluation of three-dimensional time-of-flight MR angiography. Radiology. 1990; 175:443–448. [PubMed: 2326471]
11. Nishimura DG. Time-of-flight MR angiography. Magn Reson Med. 1990; 14:194–201. [PubMed: 2345502]
12. Korosec FR, Grist TM, Polzin JA, Weber DM, Mistretta CA. MR angiography using velocity-selective preparation pulses and segmented gradient-echo acquisition. Magn Reson Med. 1993; 30:704–714. [PubMed: 8139452]
13. Shin T, Hu BS, Nishimura DG. Off-resonance-robust velocity-selective magnetization preparation for non-contrast-enhanced peripheral MR angiography. Magn Reson Med. 2013; 70:1229–1240. [PubMed: 23192893]
14. Miyazaki M, Sugiura S, Tateishi F, Wada H, Kassai Y, Abe H. Non-contrast-enhanced MR angiography using 3D ECG-synchronized half-Fourier fast spin echo. J Magn Reson Imaging. 2000; 12:776–783. [PubMed: 11050650]
15. Meuli R, Wedeen J, Frank R, Geller C, Edelman R, Rosen BR. MR gated subtraction angiography: Evaluation of lower extremities. Radiology. 1986; 159:411–418. [PubMed: 3961174]
16. Fan Z, Sheehan J, Bi X, Liu X, Carr J, Li D. 3D noncontrast MR angiography of the distal lower extremities using flow-sensitive dephasing (FSD)-prepared balanced SSFP. Magn Reson Med. 2009; 1532:1523–1532. [PubMed: 19877278]
17. Edelman RR, Sheehan JJ, Dunkle E, Schindler N, Carr J, Koktzoglou I. Quiescent-interval single-shot unenhanced magnetic resonance angiography of peripheral vascular disease: Technical considerations and clinical feasibility. Magn Reson Med. 2010; 63:951–958. [PubMed: 20373396]
18. Wright GA, Nishimura DG, Macovski A. Flow-independent magnetic resonance projection angiography. Magn Reson Med. 1991; 17:126–140. [PubMed: 2067389]
19. Brittain JH, Olcott EW, Szuba A, Gold GE, Wright GA, Irarrazaval P, Nishimura DG. Three-dimensional flow-independent peripheral angiography. Magn Reson Med. 1997; 38:343–354. [PubMed: 9339435]
20. Edelman RR, Koktzoglou I. Unenhanced flow-independent MR venography by using signal targeting alternative radiofrequency and flow-independent relaxation enhancement. Radiology. 2009; 250:236–245. [PubMed: 19092096]
21. Koktzoglou I, Edelman RR. STAR and STARFIRE for flow-dependent and flow-independent noncontrast carotid angiography. Magn Reson Med. 2009; 61:117–124. [PubMed: 19097217]
22. Brittain, JH.; Shimakawa, A.; Wright, GA.; Hargreaves, BA.; Han, E.; Stainsby, JA.; Hu, B. Non-contrast-enhanced, flow-independent, 3D peripheral angiography using steady-state free

precession at 3T; Proceedings of the 11th Annual Meeting of ISMRM; Toronto, Ontario, Canada. 2003; p. 1710

23. Çukur T, Shimakawa A, Yu H, Hargreaves BA, Hu BS, Nishimura DG, Brittain JH. Magnetization-prepared IDEAL bSSFP: A flow-independent technique for noncontrast-enhanced peripheral angiography. J Magn Reson Imaging. 2011; 33:931–939. [PubMed: 21448960]
24. Carr HY. Steady-state free precession in nuclear magnetic resonance. Phys Rev. 1958; 112:1693–1701.
25. Gronas R, Kalman PG, Kucey DS, Wright GA. Flow-independent angiography for peripheral vascular disease: Initial in-vivo results. J Magn Reson Imaging. 1997; 7:637–643. [PubMed: 9243381]
26. Kwon, KT.; Wu, HH.; Shin, T.; Kerr, AB.; Nishimura, DG.; Brittain, JH. Non-contrast-enhanced flow-independent 3D peripheral angiography with sliding interleaved concentric cylinders; Proceedings of the 20th Annual Meeting of ISMRM; Melbourne, Victoria, Australia. 2012; p. 3898
27. Liu K, Rutt BK. Sliding interleaved ky (SLINKY) acquisition: A novel 3D MRA techinique with suppressed slab boundary artifact. J Magn Reson Imaging. 1998; 8:903–911. [PubMed: 9702893]
28. Wong, EC. Magnetic resonance functional neuroimaging using interleaved SUNBURST; Proceedings of the 2nd Annual Meeting of SMR; San Francisco, California, USA. 1994; p. 25
29. Mugler, JP, III. Three-dimensional spin-echo imaging using cylindrical k-space trajectories; Proceedings of the 3rd Annual Meeting of SMR; Nice, France. 1995; p. 483
30. Ruppert, K.; Oshio, K.; Guenther, M.; Mugler, JP, III. An interleaved cylindrical k-space trajectory for rapid 3D GRE acquisitions; Proceedings of the 11th Annual Meeting of ISMRM; Toronto, Ontario, Canada. 2003; p. 208
31. Kwon KT, Wu HH, Shin T, Çukur T, Lustig M, Nishimura DG. Three-dimensional magnetization-prepared imaging using a concentric cylinders trajectory. Magn Reson Med. 2014; 71:1700–1710. [PubMed: 23818212]
32. Kwon, KT.; Hu, BS.; Nishimura, DG. Inversion-recovery-prepared sliding interleaved cylinder (SLINCY) imaging; Proceedings of the 22nd Annual Meeting of ISMRM; Milan, Italy. 2014; p. 2520
33. Kwon, KT.; Hu, BS.; Nishimura, DG. Parallel imaging for sliding interleaved cylinder (SLINCY) acquisition; Proceedings of the 22nd Annual Meeting of ISMRM; Milan, Italy. 2014; p. 4401
34. Liu K, Tanttu J, Castren A, Rutt BK. Scanning time efficient SLINKY for non-contrast MRA at low field. Magn Reson Imaging. 1999; 17:689–698. [PubMed: 10372522]
35. Gelderen, PV. Comparing true resolution in square versus circular k-space sampling; Proceedings of the 6th Annual Meeting of ISMRM; Sydney, New South Wales, Australia. 1998; p. 424
36. Bernstein MA, Fain SB, Riederer SJ. Effect of windowing and zero-filled reconstruction of MRI data on spatial resolution and acquisition strategy. J Magn Reson Imaging. 2001; 14:270–280. [PubMed: 11536404]
37. Sandgren T, Sonesson B, Ahlgren AR, Länne T. The diameter of the common femoral artery in healthy human: Influence of sex, age, and body size. J Vasc Surg. 1999; 29:503–510. [PubMed: 10069915]
38. Gold GE, Han E, Stainsby J, Wright GA, Brittain JH, Beaulieu CF. Musculoskeletal MRI at 3.0 T: Relaxation times and image contrast. AJR Am J Roentgenol. 2004; 183:343–351. [PubMed: 15269023]
39. Dharmakumar R, Hong J, Brittain JH, Plewes DB, Wright GA. Oxygen-sensitive contrast in blood for steady-state free precession imaging. Magn Reson Med. 2005; 53:574–583. [PubMed: 15723410]
40. Bangerter, NK.; Hargreaves, BA.; Brittain, JH.; Hu, BS.; Vasanawala, SS.; Nishimura, DG. 3D fluid-suppressed T2-prep flow-independent angiography using balanced SSFP; Proceedings of the 12th Annual Meeting of ISMRM; Kyoto, Japan. 2004; p. 11
41. Nishimura DG, Macovski A, Pauly JM, Conolly SM. MR angiography by selective inversion recovery. Magn Reson Med. 1987; 4:193–202. [PubMed: 3561250]

42. Nezafat R, Ouwerkerk R, Derbyshire AJ, Stuber M, McVeigh ER. Spectrally selective B1-insensitive T2 magnetization preparation sequence. Magn Reson Med. 2009; 61:1326–1335. [PubMed: 19319903]

43. Wright HP, Osborn SB. Effect of posture on venous velocity, measured with ^{24}NaCl. Br Heart J. 1952; 14:325–330. [PubMed: 14944721]

44. Parker DL, Yuan C, Blatter DD. MR angiography by multiple thin slab 3D acquisition. Magn Reson Med. 1991; 17:434–451. [PubMed: 2062215]

45. Lustig M, Pauly JM. SPIRiT: Iterative self-consistent parallel imaging reconstruction from arbitrary k-space. Magn Reson Med. 2010; 64:457–471. [PubMed: 20665790]

46. Du YP, Parker DL, Davis WL, Cao G. Reduction of partial-volume artifacts with zero-filled interpolation in three-dimensional MR angiography. J Magn Reson Imaging. 1994; 4:733–741. [PubMed: 7981519]

47. Robison RO, Blatter DD, Parker DL, Barney WW, Perry DM, Goodrich KC. Reduction of slab boundary artifact with multiple overlapping thin slab acquisition in MR angiography of the cervical carotid artery. J Magn Reson Imaging. 1994; 4:529–535. [PubMed: 7949677]

48. Morrell G, Spielman D. Dynamic shimming for multi-slice magnetic resonance imaging. Magn Reson Med. 1997; 38:477–483. [PubMed: 9339449]

49. Graves MJ, Wong P, Priest AN, Black RT, Lomas DJ. Slice offset frequency and shim adjustment for interactive steady-state free-precession (SSFP) imaging. J Magn Reson Imaging. 2009; 29:1230–1233. [PubMed: 19388102]

50. Kwon, KT.; Kerr, AB.; Hu, BS.; Nishimura, DG. Sliding interleaved cylinder (SLINCY) imaging with dynamic center frequency adjustment; Proceedings of the 21st Annual Meeting of ISMRM; Salt Lake City, Utah, USA. 2013; p. 555

51. Larson PZ, Gurney PT, Nishimura DG. Anisotropic field-of-views in radial imaging. IEEE Trans Med Imaging. 2008; 27:47–57. [PubMed: 18270061]

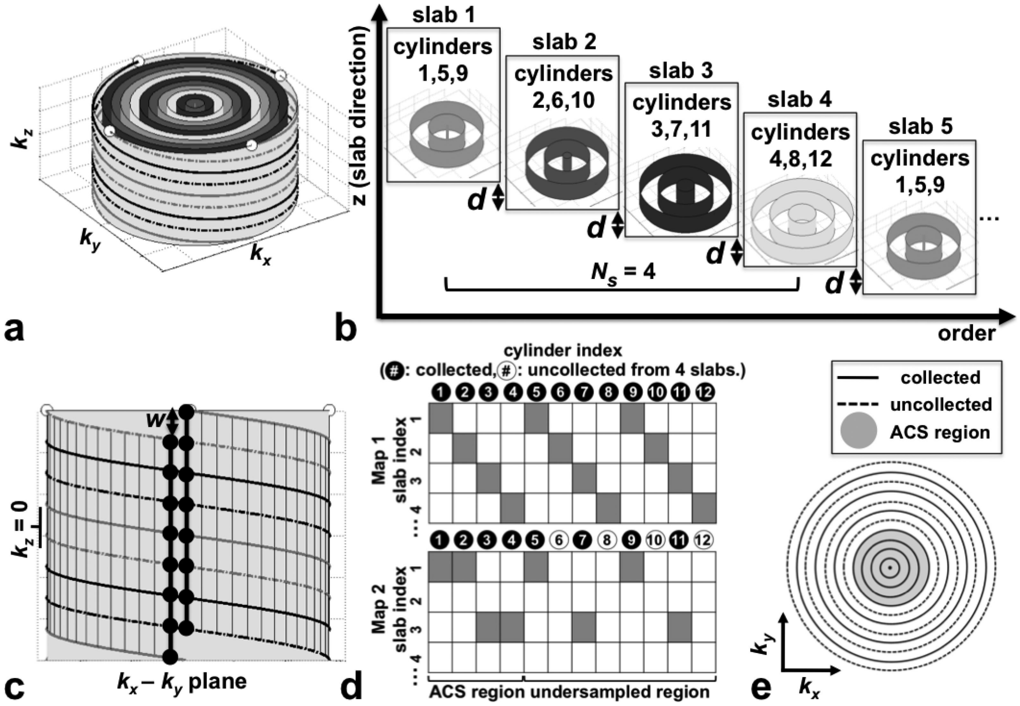

FIG. 1.

SLINCYL acquisition. **a:** 3D concentric cylinders trajectory with N_{cy} = 12, N_{intlv} = 4, and N_{rev} = 2. The outermost cylinder is depicted with its surrounding helical interleaves. (white dots: end points of interleaves). Cylinders with the same color belong to the same subset as shown in **(b)**. **b:** Data acquisition scheme. A subset of the cylinders is collected at each slab in an interleaved way, which repeats every N_s = 4 slabs. The slab location is incremented by a distance d equal to the resolution in z. **c:** View of the outermost cylinder in **(a)** from the side. With N_{samp} (= 112) chosen as an integer multiple of N_{slice} (= 8), each sampling point is aligned in the k_z direction with other $N_{slice} - 1$ (= 7) points as highlighted by two bold vertical lines (black dots: sampling points). Lines are shifted (w) with respect to each other in k_z, which necessitates a linear phase correction in z after applying a 1D inverse Fourier transform in k_z. **d:** Acquisition maps for N_s = 4 slabs (colored cells: locations cylinders are acquired). While the fully sampled map (top) collects a full set of 12 cylinders from four slabs, the undersampled map (bottom, reduction factor R = 2) does not collect cylinders 6, 8, 10, and 12 by skipping slabs with even indices. As the ACS region, the four innermost cylinders are fully sampled. **e:** The corresponding undersampling pattern of the k-space data in each slice. Rings 6, 8, 10, and 12 are uncollected as expected.

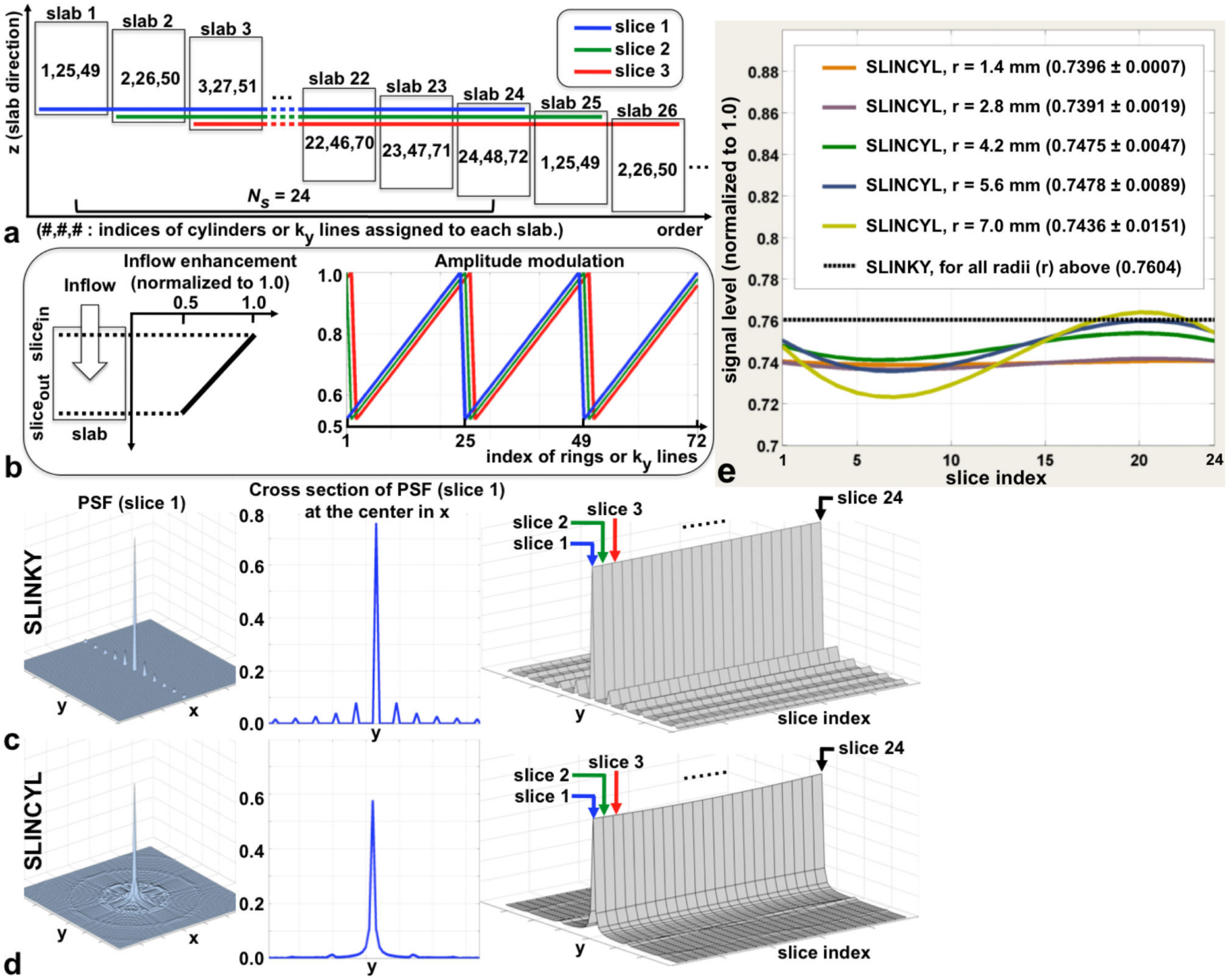

FIG. 2.

SLINKY vs. SLINCYL. **a:** Data reconstruction scheme of SLINCYL and SLINKY with N_s = 24 and 72 cylinders or k_y lines. As highlighted with colored lines, relevant hybrid slices are selected out of N_s consecutive slabs to reconstruct each slice. **b:** A sawtooth shape of periodic (period = N_s) k-space amplitude modulation (right) for each colored slice in **(a)** caused by in flow enhancement (left). The modulation pattern is circularly shifted for different slices, which repeats every N_s slices. **c,d:** The magnitude of the PSF of slice 1 (left), its cross section (middle), and cross sections of the PSFs of N_s = 24 slices stacked together (right). Across the 24 slices, the PSFs of SLINCYL **(d)** consistently show more distributed artifacts than SLINKY **(c)**. **e:** Signal levels across N_s = 24 slices with different vessel radii. Although not as constant as SLINKY, SLINCYL also provides relatively uniform signal levels for vessels with radius up to 7 mm.

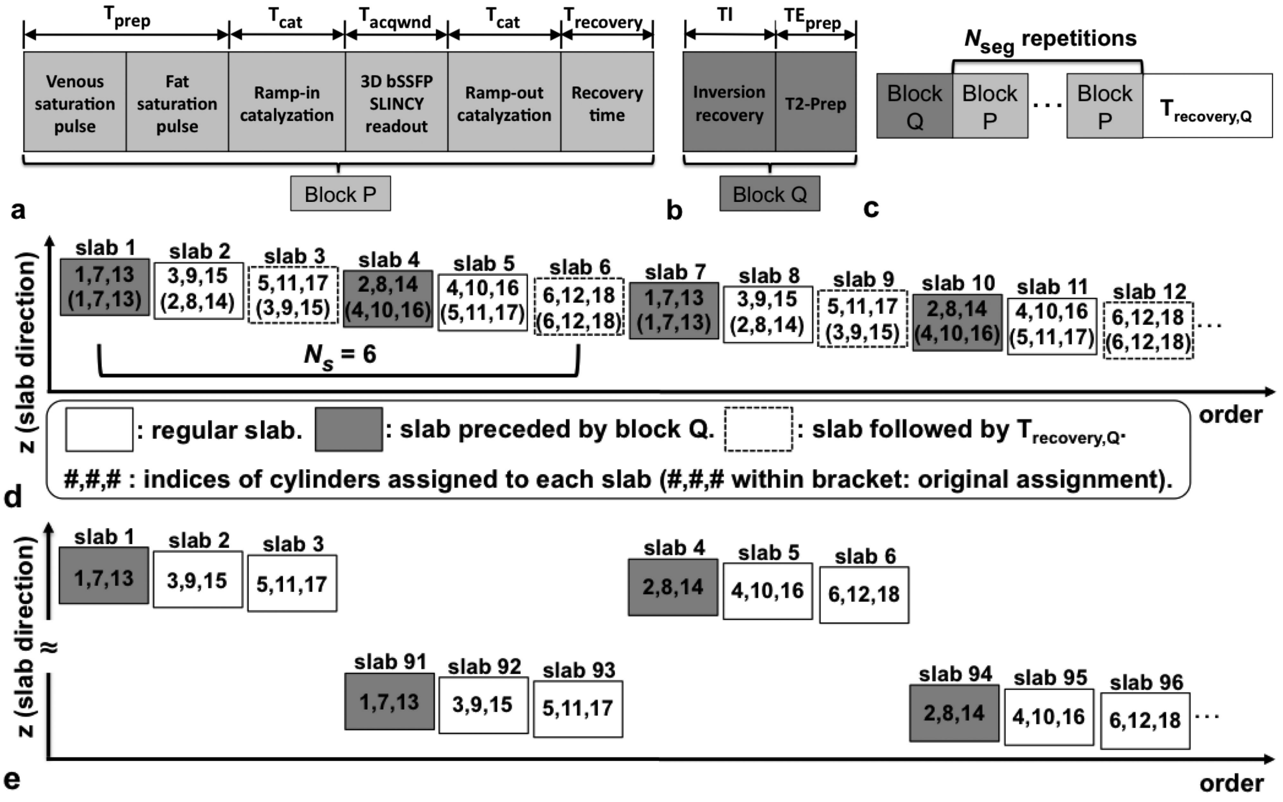

FIG. 3.

Pulse sequence diagrams of SLINCYL MRA. **a:** Basic block P. **b:** Additional block Q for fluid suppression. **c:** Pulse sequence diagram of each slab. N_{seg} repetitions of block P are surrounded by block Q and $T_{recovery,Q}$ for fluid suppression. **d:** modified sequence for fluid-suppression (illustrated with N_s = 6, N_g = 3, and N_{cy} = 18). Block Q (before each dark slab) and $T_{recovery,Q}$ (after each dashed slab) pairs are applied once per every N_g = 3 slabs. In addition, the assignment of an interleaved subset of cylinders to each slab is modified such that slabs acquired immediately after blocks Q collect the N_s/N_g (=2) innermost cylinders. This scheme captures the transient contrast more effectively than the case with the original assignment (indices within brackets). **e:** Further modified sequence for fluid-suppression. A total of 180 slabs are acquired by interleaving the lower (slab indices 91 to 180) and upper (1 to 90) half the slabs. In this way, no overlap exists between any adjacent sets of N_g = 3 slabs and the explicit recovery time $T_{recovery,Q}$ is no longer necessary.

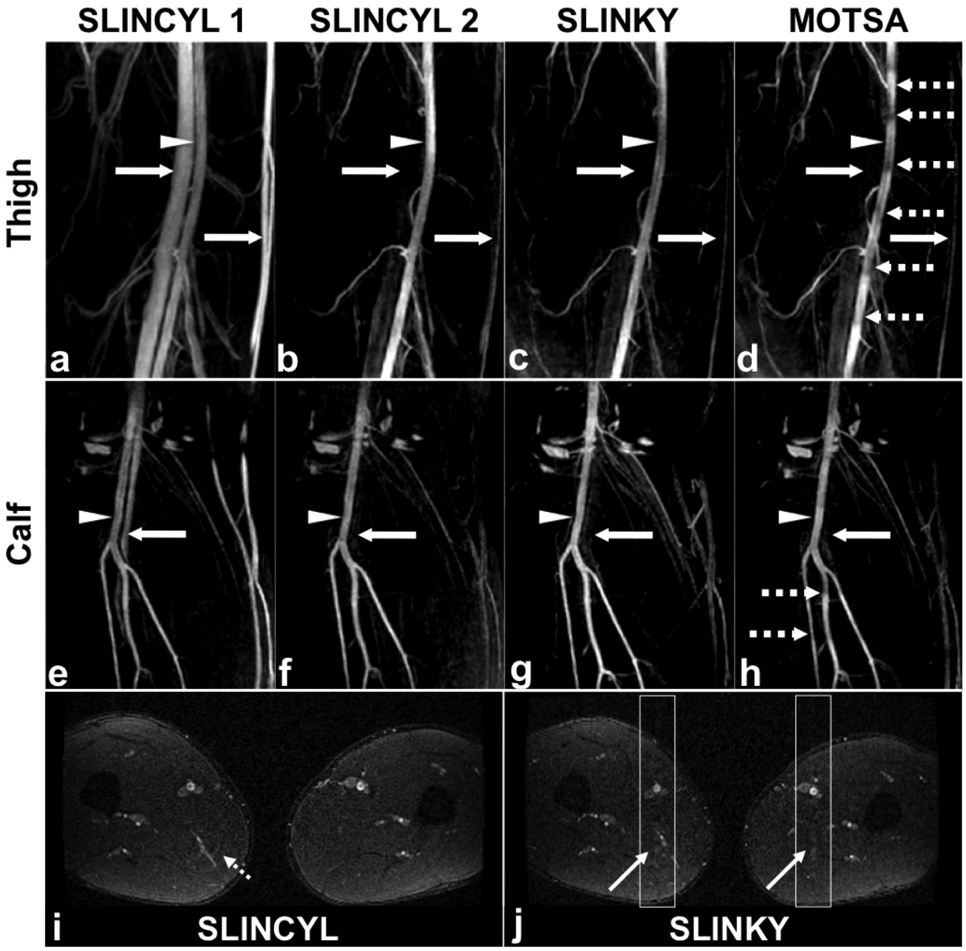

FIG. 4.

SLINCYL, SLINKY, and MOTSA MRA of thighs and calves of healthy subjects. Compared to SLINCYL without venous saturation pulse **(a,e)**, SLINCYL with venous saturation pulse **(b,f)** significantly improves contrast between arteries (arrow heads) and veins (solid arrows) without loss of arterial signal. Compared to MOTSA **(d,h)**, both SLINKY **(c,g)** and SLINCYL successfully suppress the venetian blind artifacts (dashed arrows) and provide similar artery-vein contrast. However, SLINCYL achieves this with shorter scan times than SLINKY, as summarized in Table 2. The ghosting artifacts of the superficial femoral arteries are prominent with SLINKY **(j)**, which are aligned in the A/P direction in the component axial slice (diagonal solid arrows). For SLINCYL **(i)**, the artifacts are distributed over the *x*-*y* plane (diagonal dashed arrow), which is consistent with the simulation results in Fig. 2.

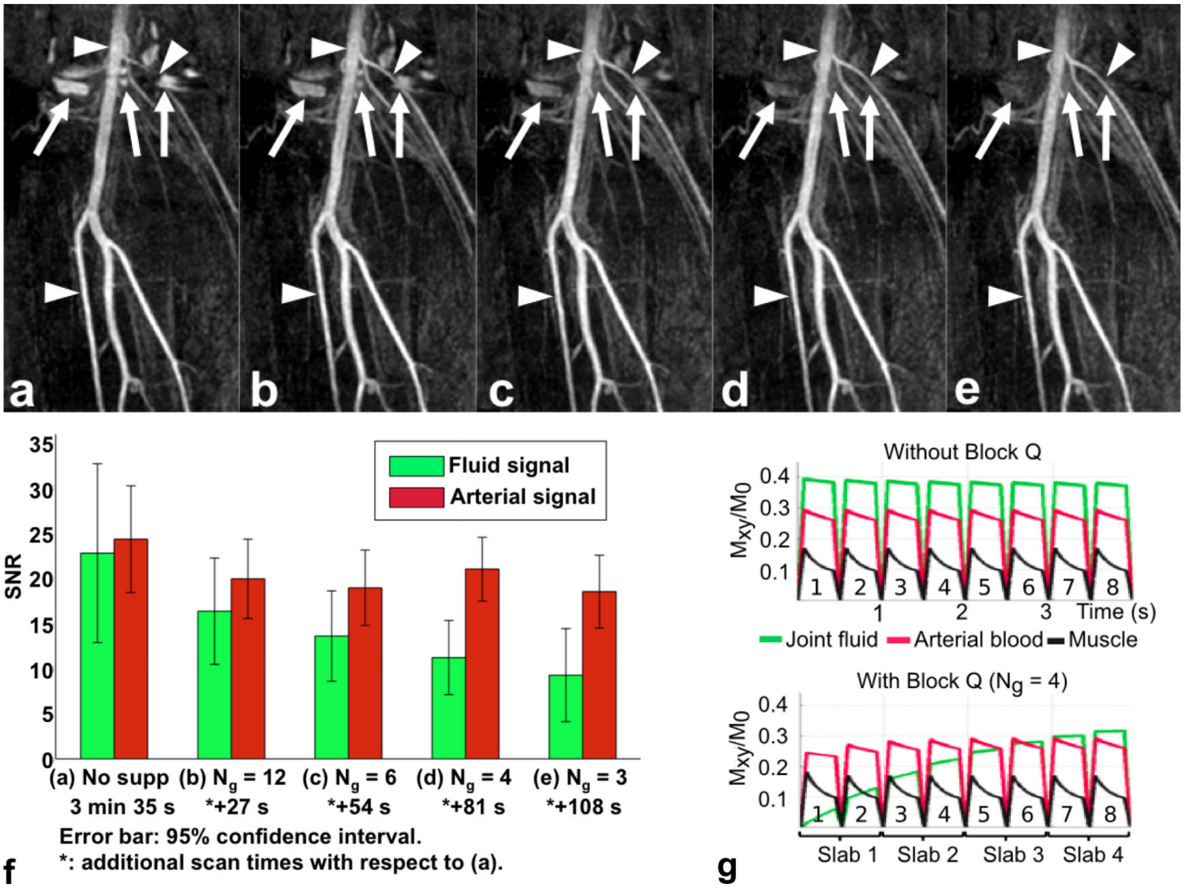

FIG. 5.

SLINCYL MRA of the calves of a healthy subject with/without block Q and corresponding Bloch simulations. Compared to the acquisition without block Q **(a)**, the acquisitions with block Q (**b:** $N_g = 12$, **c:** $N_g = 6$, **d:** $N_g = 4$, **e:** $N_g = 3$) provide better depiction of arterial signals (arrowheads) due to the suppression of fluid signals (arrows) around the knee joint. The degree of fluid suppression is further improved as block Q is applied more frequently (i.e., with smaller N_g). **f:** SNR of fluid and arterial signals and scan time for each case. **g:** Bloch simulations of transient bSSFP signals corresponding to **(a)** (top) and **(d)** (bottom). Similar to the in vivo result, joint fluid (green) is much suppressed with block Q applied ahead of every $N_g = 4$ slabs, particularly for the first slab that collects the six innermost cylinders.

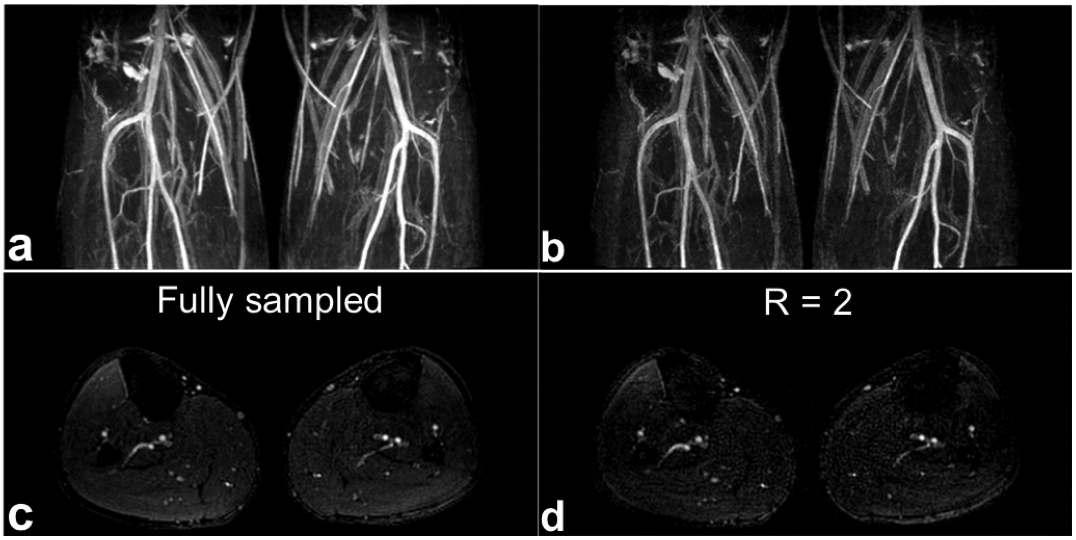

FIG. 6.

SLINCYL MRA of the calves of a healthy subject with a fully sampled and an undersampled acquisition. In addition to coronal MIP images **(a,b)**, representative axial slice **(c,d)** from each acquisition is shown. The prospectively undersampled (R = 2) case reconstructed with the proposed parallel imaging method **(b,d)** shows comparable image quality to the fully sampled case **(a,c)** other than the decrease in SNR. The main arteries (popliteal, anterior tibial, posterior tibial, and peroneal) are well depicted in both cases.

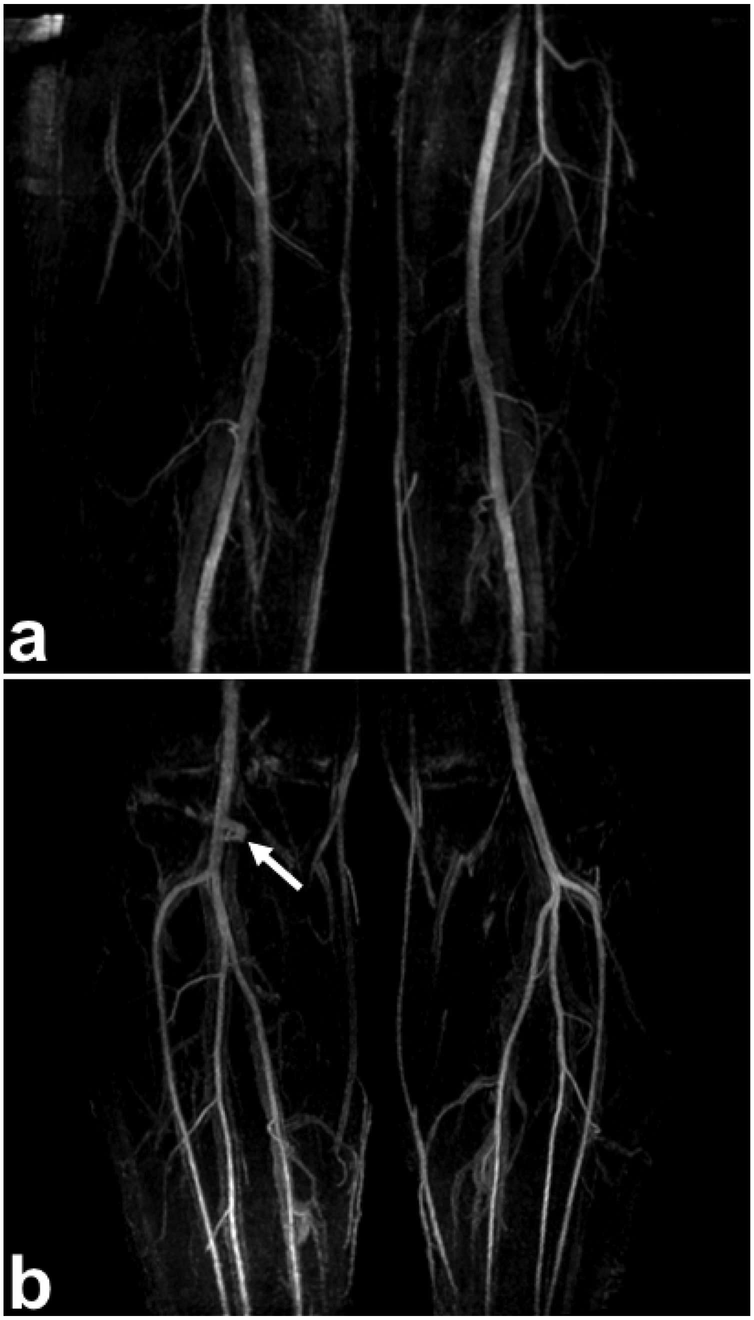

FIG. 7.

Two-station SLINCYL MRA of the thighs **(a)** and calves **(b)** of a healthy subject. Both parallel imaging ($R = 2$) and fluid suppression ($N_g = 4$) were applied. The main arteries (femoral, popliteal, tibial, and peroneal) are well depicted across the FOV with good overall background suppression. Some fluid signal around the knee joint (arrow) was not sufficiently suppressed due to the increased number of readouts per slab accompanied with a shorter TR.

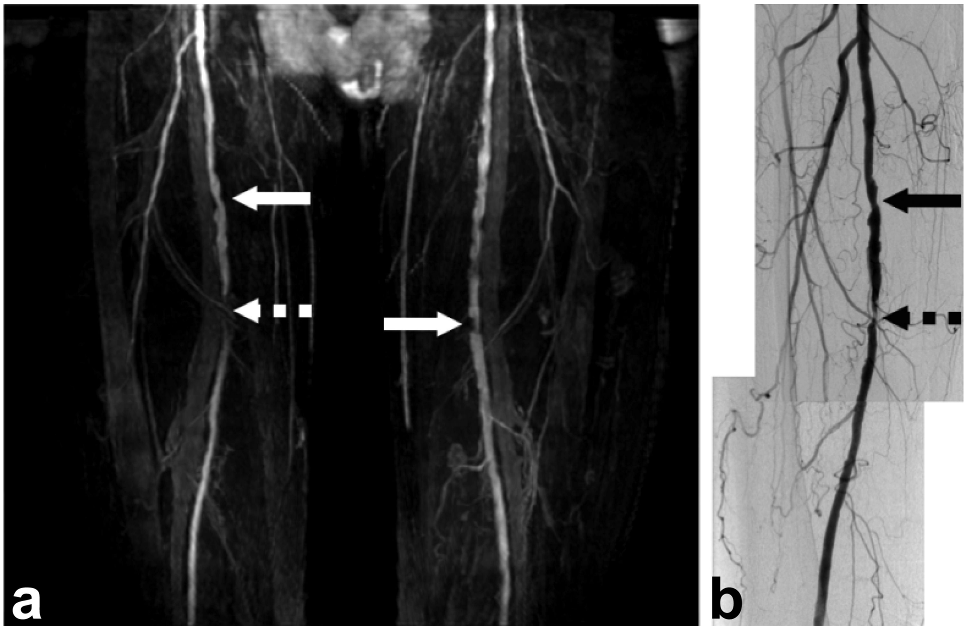

FIG. 8.

SLINCYL MRA **(a)** of the thighs of a 75-year-old male patient, compared with digital subtraction angiography (DSA, right leg only) **(b)**. Stenoses at the superficial femoral arteries (arrows) are well identified on both the SLINCYL MRA and DSA images.

Table 1

Sequence Parameters for Each Slab of SLINCYL.

Parameter	**Thighs**	**Calves**
Resolution	1.4 mm isotropic	1.2 mm isotropic
FOV [A/P, R/L, S/I]	34 (17) × 34 × 4.5 cm^3	34 (17) × 34 × 3.8 cm^3
Flip angle/TR	70°/6.8 ms (5.4 ms)	60°/7.2 ms (5.8 ms)
$N_{cy}/N_{intlv}/N_{rev}/N_{samp}$	120(·)/16(·)/2(·)/768(240)	144(·)/16(·)/2(·)/832(288)
$N_{slice}/N_s/N_{seg}$	32/24/2(3)	32/24/2(3)
T_{acqwnd} (Fig. 3a)	272 ms (297 ms)	346 ms (383 ms)
Scan time	1.11 s (1.63 s)	1.28 s (1.95 s)

(#): Corresponding numbers for SLINKY if different from SLINCYL.

(·): Not available to SLINKY.

N_{cy}: # of cylinders per slab, N_{intlv}: # of helical interleaves per cylinder.

N_{rev}: # of revolutions per interleaf, N_{samp}: # of sampling points per interleaf.

N_{slice}: # of slices per slab, N_s: # of interleaved subsets of cylinders or k_y lines.

N_{seg}: # of readout segments per slab, N_{slab}: # of slabs.

Table 2

Comparisons of SNR and Scan Times of SLINCYL, SLINKY, and MOTSA.

		SLINCYL 1[a]	**SLINCYL 2**[b]	**SLINKY**	**MOTSA**
Thighs	SNR_{artery}:	45.96±5.87	46.87±5.94	49.01±5.93	41.64±4.64
	SNR_{vein}:	39.81±6.15	17.78±1.65	15.29±1.81	16.16±2.05
	SNR_{muscle}:	8.94±1.31	9.21±1.11	7.54±1.00	7.20±1.06
	Scan time:	3 min 1 s	3 min 6 s	4 min 33 s	4 min 33 s
Calves	SNR_{artery}:	22.56±2.36	24.22±3.00	24.14±2.51	24.31±2.57
	SNR_{vein}:	20.50±2.56	9.81±1.43	9.91±1.45	9.94±1.11
	SNR_{muscle}:	5.60±0.93	6.16±1.01	6.03±1.02	5.56±1.04
	Scan time:	3 min 30 s	3 min 35 s	5 min 28 s	5 min 28 s
			1 min 57 s[*]		

[a] Without/with venous saturation pulse.

[b] Without/with venous saturation pulse.

[*] With parallel imaging (Fig. 6).